Journal Pre-proof

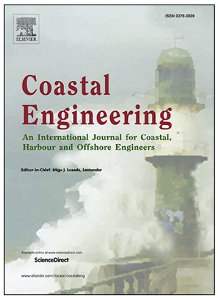

Interactions between swell and colinear wind short crested waves, following and opposing

Fabio Addona, Maria Clavero, Luca Chiapponi, Sandro Longo

PII: S0378-3839(24)00197-2
DOI: https://doi.org/10.1016/j.coastaleng.2024.104649
Reference: CENG 104649

To appear in: *Coastal Engineering*

Received date : 18 July 2024
Revised date : 24 October 2024
Accepted date : 25 October 2024

Please cite this article as: F. Addona, M. Clavero, L. Chiapponi et al., Interactions between swell and colinear wind short crested waves, following and opposing. *Coastal Engineering* (2024), doi: https://doi.org/10.1016/j.coastaleng.2024.104649.

In memory of Miguel A. Losada Rodríguez

Interactions between swell and colinear wind short crested waves, following and opposing

Fabio Addona[1a], Maria Clavero[b], Luca Chiapponi[a], Sandro Longo[a]

[a]*Department of Engineering and Architecture, University of Parma, Parco Area delle Scienze, 181/A, Parma, 43124, Italy*
[b]*Andalusian Institute for Earth System Research, Universidad de Granada, Av. del Mediterráneo s/n, Granada, 18006, Spain*

Abstract

When wind blows over a water surface during a swell, it generates short-crested, three-dimensional waves that interact with the underlying flow field through a mechanism that ultimately increases the average energy. In the present work, two test cases in which wind is flowing following and opposing a swell are analysed with experiments and are compared with wind-wave-only and swell-only cases. The analysis of the free surface fluctuation and of the flow field, with the three components of fluid velocity measured at the same time through a stereo particle image velocimetry system, leads to an accurate quantification of the energy distribution, of the structure of the oscillating, fluctuating (due to wind-waves) and turbulent kinetic energy, without assumptions on the structure of the flow. The findings demonstrate that the transverse dynamics is a pivotal factor in the transfer of energy in the near-free surface domain, and elucidate the energy transfer between wind-waves and swell. The results also confirm the reduction of oscillating kinetic energy of the swell in the presence of short wind-waves, a process interpreted with different possible mechanisms. There is evidence of the enhancement of wind action in the presence of swell compared to that in the case of wind-waves-only, confirming that energy transfer from the wind to the sea is enhanced when wind flows over a swell. Consequently, when the fetch is influenced by swells generated or propagated from different regions, and during multi-peak sea storms, wave generation models should account for this amplification.

[1]Corresponding author

Keywords: wind-waves, swell, turbulence

1. Introduction

Oceans cover most of the Earth's surface, and their interaction with the lower atmosphere is crucial for the exchange of mass, momentum, heat and chemicals (Semedo [1]).

Common observations of wind blowing over the Earth's surface include the compresence of waves and currents at different scales (Sullivan and McWilliams [2]). The airflow exerts normal and tangential stresses on the sea surface, causing wave generation, growth, and dissipation through several mechanisms that are not yet fully understood (Jeffreys [3], Miles [4], Phillips [5], Belcher et al. [6]). On the other hand, wind-generated waves strongly influence airflow by inducing air-flow separation and altering the distribution of wind-coherent stresses along the wave phase (Buckley and Veron [7, 8], Buckley et al. [9], Yousefi et al. [10]). When offshore wind-generated waves travel far from their generation area, dissipation, dispersion and non-linear wave-wave interactions redistribute energy across the spectrum (Hasselmann [11, 12, 13], Hasselmann et al. [14]). As a consequence, waves become longer, with narrow directional spread and more regular. For these scales the direct effect of surface tension is irrelevant, and the only restoring force is gravity. The resulting wave field is called a swell.

A frequent situation in the field is wind blowing over swell, which can potentially have any propagation direction angle with respect to the air flow. In laboratory studies, 2D wave flumes and wind tunnels are used to reproduce wind-wave interactions, thus only situations where wind blows either in following or in opposite directions are considered, and wind and waves are colinear. Mitsuyasu [15] was one of the first researcher to study the interaction of short wind-waves and mechanically-generated regular waves, showing that swell can attenuate wind-generated waves if the former are sufficiently steeper. Guided by those results, Phillips and Banner [16] proposed a mechanism which enhances wind-waves breaking at the crest of the swell. Succeeding researchers have shown that the mechanism depicted by Phillips and Banner was not strong enough at high wind speeds (Wright [17]), and suggested other mechanisms for the wind-waves attenuation, such as wave-wave interaction or swell-wind coupling (Masson [18], Chen and Belcher [19]).

Many researchers have been involved in the study of the flow field beneath water waves in the presence of wind (see, among the first works, Wu [20], Shemdin [21], Howe et al. [22], Bliven et al. [23]). Cheung and Street [24] carried out extensive experimental work on mechanically generated waves in the presence of a following wind. In their experiments, they observed a kinetic energy transfer from the wave-induced component to the mean flow, and suggested a coupling between turbulence and wave-induced motions. Other studies focused on the attenuation of swell due to the presence of an opposing wind, although there is no agreement on the wave decay rate (Peirson et al. [25], Mitsuyasu and Yoshida [26]).

Recently, a series of papers have documented experiments in a more complex configuration, with partially-reflected mechanical waves with colinear wind in several configurations, i.e., following wind, no wind, and opposing wind (Addona et al. [27, 28], Addona and Chiapponi [29], Addona [30]). The main interest was to study the effects of wave reflection, which can be relevant in coastal areas due to the presence of the shorelines, bottom slopes and breakwaters (Elgar et al. [31], Baquerizo et al. [32]).

A problem that has been addressed by various techniques, none of which have solved it in full, is the separation of the different scales, starting with the velocity components of wind, swell and turbulence. The contribution of Thais and Magnaudet [33], which is thorough and detailed with regard to the interpretation of the results, seems to be one of the most consistent and coherent, both in its hypotheses and in the discussion of the data obtained. This topic is broader, as it includes the propagation of surface turbulence in the water column, as well as the coupling between turbulence, velocity fluctuations associated with wind-waves, and periodic oscillating components of swell. Some aspects of the more general scenario have already been addressed to a greater or lesser extent, but without a holistic approach. For example, the interaction of turbulence with the surface was treated experimentally in Dabiri and Gharib [34] to estimate the correlation between surface deformation and the momentum flux, including vorticity, near the surface. The interaction between partially-reflected waves and an opposing wind, with a combination of following-opposing wind acting on the incident/reflected waves, was experimentally described in Addona et al. [28]. The transition to turbulence in wind drift layers has been carefully described in a recent paper by Wagner et al. [35]. The structure of the flow field, the balances of momentum and of energy and the time evolution of a breaking wave on a berm have been studied by Clavero et al. [36] and in Longo et al. [37] via 3D particle tracking velocimetry, with a temporal and spatial resolution that is sufficient for an adequate and coherent analysis of physical processes. It is noteworthy that the latter two studies are within the limited number of experimental research projects based on the three-dimensional measurements of velocity, as observed at different points at the same time. Several studies are based on two-dimensional measurements and on numerical simulations.

Despite the efforts, general analyses about the energy flux, the processes that transform short-crested wind-waves into long-crested waves, and the role of macrostructures in modulating intermediate and small structures are still lacking and need appropriate analysis. In this paper, a flow field in the presence of wind-waves superimposed on regular mechanically generated waves, with the wind blowing in the same or opposite direction of propagation of the regular waves, is analysed. Two experiments in the presence of only wind and only mechanically generated regular waves were also performed for comparison and overall validation of the results. The measurements were made with a Stereo Particle Imaging Velocimetry (S-PIV) device, which allows the reconstruction of the three velocity field components at the nodes of a regular grid on one plane. In many respects, the measurements are similar to those of Thais and Magnaudet [33], who reconstructed the three velocity components at a series of measurement volumes along a vertical line via laser Doppler. The main difference is that in the present activity, the three velocity components are recorded simultaneously, rather than in velocity pairs being recorded by rotating the laser probe along a vertical axis and at different times for each recording volume. The availability of simultaneous data in a plane makes the statistics more consistent and allows a broader view of the structure of the entire flow field. Furthermore, this approach allows for the evaluation of velocity and stress gradients in the plane of S-PIV measurements, which is left for future work due to the large number of results reported in the following sections.

The manuscript is organized as follows. The experimental activity and facility are described in §2, and §3 is dedicated to data analysis and to the decomposition methods. In Section §4, the swell flow field, the oscillating kinetic energy (OKE), and the time average velocity are analysed. In Sections §5 and §6, the short wind-waves flow field (including the wind-waves kinetic energy, WKE) and turbulence (including the turbulent kinetic energy, TKE) are evaluated, respectively, while the total energy content is discussed in §7.

The conclusions are provided in the last section. Some additional details are reported in Appendix A, Appendix B and Appendix C.

2. The experiments

The experiments were conducted in an Ocean-Atmosphere Interaction flume (CIAO) located in Granada, Spain (see Addona [38] for details). The flume, with a length of 16 m, width of 1.0 m, and height of ≈ 2 m (≈ 0.65 m is the still water depth), allows for the generation and coupling of mechanically (paddle) generated waves, wind-generated waves, colinear currents, and rain. The CIAO is equipped with a PC-controlled active system for wave generation/absorption based on two paddles on opposite sides of the flume.

The displacement of the water surface was measured with eight UltraLab ULS 80D (US) ultrasonic probes, sensor model USS635, with a data rate of 75 Hz. The water velocity was measured with the Stereo Particle Image Velocimetry technique (S-PIV), and the velocity of the wind was measured with a Pitot tube.

The S-PIV measurements were made in a single downstream section, with a fetch of 9 m and with Field of View (FOV) of $140 \times 140\,\text{mm}^2$, a data rate of 7.25 Hz in a frame-straddling mode, acquiring approximately 1000 pairs of frames for each camera and each run. The velocity components are u, v and w, which are aligned with the horizontal $x-$axis, with the vertical $y-$axis and with the spanwise $z-$axis, with the origin at the still water level. A sketch of the experimental setup is shown in Figure 1.

In the following, we will refer to the monochromatic mechanically generated waves as “swell", and to waves generated by the local wind action as “wind-waves"

For the purposes of the present analysis, we will only consider four experiments, one with wind following the swell, a second with wind opposing the swell, and for reference a third and a fourth with only wind and only swell, respectively. The swell has a nominal wave height $H_m = 50\,\text{mm}$ and wave period $T_m = 1.45\,\text{s}$ for all the experiments where mechanically-generated waves are present (“nominal" refers to the value imposed on the generation system). Since the water depth was $h = 0.65\,\text{m}$, the swell is in intermediate depth. A full list of the parameters for the four experiments is presented in Table 1.

Figure 2 shows the measured instantaneous free surface elevation time series for the four experiments in the section where Sensor US4 is installed,

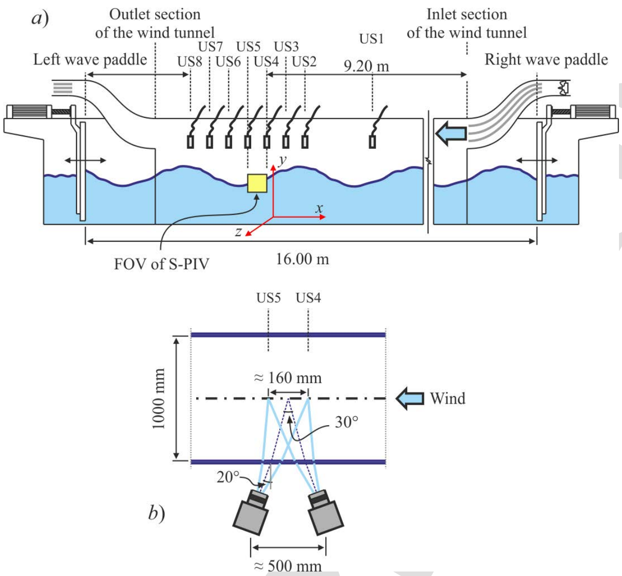

Figure 1: The experimental flume and schematic of the probes and of the two S-PIV cameras. *a*) Side view of the flume, *b*) top view.

and figure 3 shows the spectral power density of surface elevation fluctuations in the same section. For the experiment with wind-waves-only, grouping can be observed, while there is no apparent difference between the free surface elevation time series for the wind following/opposing the swell.

The spectra clearly show the separate contributions of the wind-generated waves and of the swell. The presence of a swell increases the peak of the wind-waves with respect to the wind-waves alone, while reducing the frequency of the peak from ≈ 3 Hz to ≈ 2 Hz, to a greater extent for the following waves than for the opposing waves. The second harmonic of swell is present in the following waves case only.

Wind speed was measured with a Pitot static tube at several vertical positions, averaging over 60 s. The wind speed vertical profiles are shown in figure 4. The friction velocity in water u_{*water}, assumed to be the velocity scale for most variables, is calculated by first estimating the friction velocity in air, u_{*air}, which is obtained by interpolating the measured velocities using

Exp.	h (mm)	$U_{w\infty}$ (m s^{-1})	H_m (mm)	T_m (s)	L_{exp} (m)	H_{rms} (mm)	u_{*air} (mm s^{-1})	c/u_{*air}	u_{*water} (mm s^{-1})	K_r	H_{w-rms} (mm)	T_{w-rms} (s)	
1	643	−7.25	-	-	-	18.4	520	-	18.2	-	18.4	0.34	wind only
2	648	-	50	1.45	2.96	49.1	-	-	-	0.055	-	-	wave only
3	650	-9.40	50	1.45	2.94	50.8	670	3.02	23.5	0.074	27.1	0.43	opposing
4	649	-10.25	50	1.45	2.91	52.3	780	2.57	27.4	0.083	26.7	0.46	following

Table 1: Parameters of the experiments. h is the still water depth, $U_{w\infty}$ is the asymptotic wind speed, H_m is the nominal wave height of the mechanically generated regular waves, T_m is their nominal wave period, L_{exp} is the measured wave length (based on cross-correlation of the free surface elevation time series at different sections), c/u_{*air} is the wave age, H_{rms} is the root-mean-square height measured in the section where S-PIV is performed, $u_{*air,water}$ is the friction velocity in the air/water side, K_r is the reflection coefficient, H_{w-rms} is the estimated wind-wave height (root-mean-square value), and T_{w-rms} is the estimated wind-wave period (root-mean-square value). The slope of the wave in exp. 2 is $H_m n = 0.106$, where $n = 2\pi/L_{exp}$ is the wavenumber. Regular mechanically generated waves are at an intermediate depth.

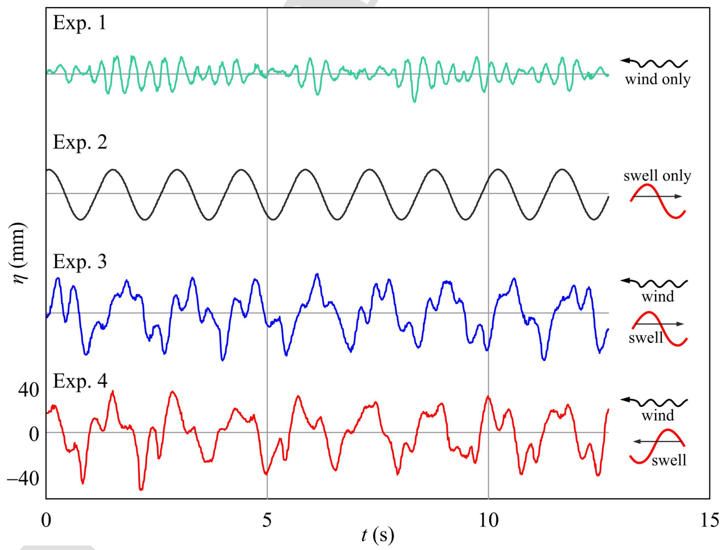

Figure 2: The measured free surface elevation time series in Section US4.

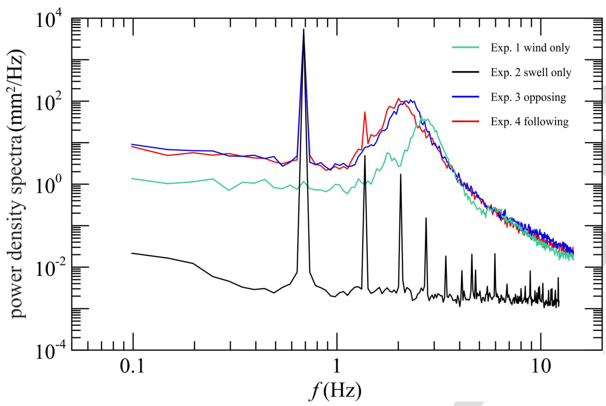

Figure 3: The power density spectra of the measured free surface elevation fluctuations in Section US4, with 70-100 degrees of freedom.

a logarithmic profile:

$$\frac{U_w}{u_{*air}} = \frac{1}{k} \ln\left(\frac{y}{y_0}\right). \quad (1)$$

Here y_0 is the geometric roughness and κ is the von Kármán constant. By assuming a tangential stress balance at the interface (Thais and Magnaudet [33]), the following expression can be obtained:

$$u_{*water} = \sqrt{\frac{\rho_{air}}{\rho_{water}}} u_{*air}, \quad (2)$$

where $\rho_{air,water}$ are the air and water densities, respectively.

The analysis of uncertainty for the measured variables is reported in the Appendix A.

Data presentation and interpretation refer to dimensionless values, with the length scale represented by H_{rms} and the velocity scale represented by u_{*water}, except in the swell-only case, for which the velocity scale is $H_{rms}/T_m = 31.4\,\mathrm{mm\,s^{-1}}$ (there is no wind blowing, so the air/water friction velocity is not defined).

3. Data analysis

The standard analysis requires the identification of the interface by separating water and air pixels, and the application of time-averaging, phase-

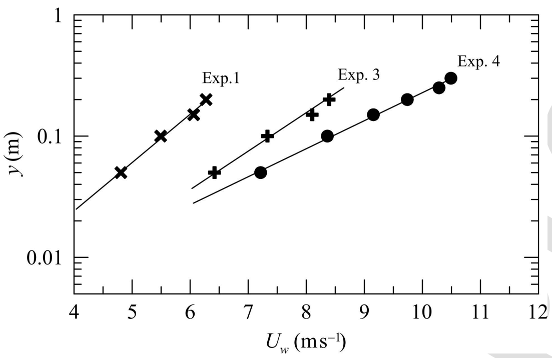

Figure 4: The experimental wind velocity profiles for the three different experiments.

averaging, and phasic-averaging operators. This last operator accounts for presence/absence of water in the volume of measurement.

To avoid interpreting the flow field between the crest and the trough with a fixed coordinate system, a mobile frame was adopted, and velocity data were interpolated onto a rectangular grid with points in the same row equidistant from the instantaneous water level, as shown in figure 5. In the present experiments the water level was manually identified frame by frame on the S-PIV sequence of images. This coordinate system is similar to the wave-following coordinate system adopted for the air side in Grare et al. [39]; a streamline (curvilinear) coordinate system was recently adopted in Xuan and Shen [40] for the numerical simulation of the interaction between waves and turbulence, which has the advantage of resolving the processes that occur on a scale smaller than the wave period (or wavelength).

After mapping, the variables of interest were calculated and, for some of them, remapped to the original coordinate system for a clearer visualisation. The estimated values of, e.g., turbulent kinetic energy and Reynolds stresses are available up to the free surface without the need for extrapolation or the adoption of specific phasic-average operators. This procedure introduces a further element of uncertainty, due to the identification of the free surface. However, the nature of the processes involved, as well as the way in which they are interpreted in terms of averaging, insures that the increase in uncertainty is balanced by the enhanced coherence of the data analysis achieved through averaging over the new mesh.

The phase axis is inverted for exp. 4 to correctly represent the upwind

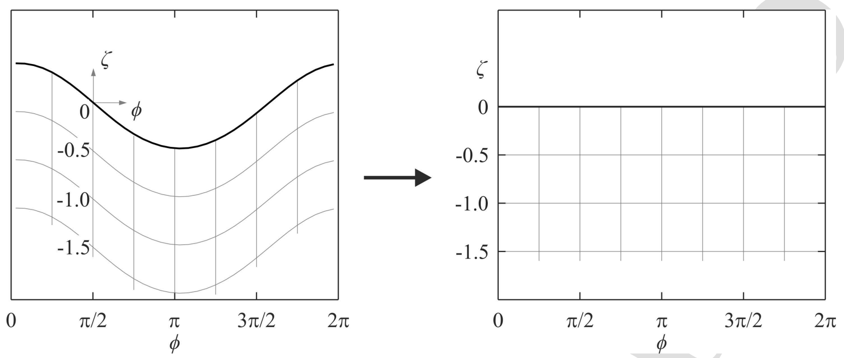

Figure 5: The wave following frame $\zeta - \phi$ is mapped to a rectangular grid. ζ is the dimensionless vertical coordinate following the free surface, ϕ is the phase of the swell with origin at the crest, increasing in the direction of propagation of the wave.

and downwind domains, as the wind is always in the negative direction of the $x-$axis and the swell propagates in the positive direction for expts 2–3 and in the negative direction for exp. 4.

The main obstacle to interpreting the velocity data is the separation of the velocity components due to swell, wind-waves and turbulence. In this regard, it should be noted that the methods proposed in the past make some assumptions, i.e., they often require the selection of thresholds that are not objectively defined. For instance, the filtering method, widely used by several researchers, requires the selection of a band of frequencies across the peaks of the spectrum, with a bandwidth that is not uniquely defined. Thais & Magnaudet's [41] triple decomposition is based on the assumption of the nondispersive behaviour of all the wave components travelling at the phase speed of the wave corresponding to the frequency peak of the spectrum. Even the definition of the turbulent component varies, with the turbulent component calculated using different methods depending on whether only wind-waves or wind-waves and swell are present. In the latter case, the linear superposition technique developed by Donelan et al. [42] and used by Thais and Magnaudet [41] makes it possible to separate the velocity fluctuations into wind-waves velocity components and turbulent fluctuations with respect to the phase-averaged orbital velocities.

In the presence of regular waves plus wind-waves, further separation is performed by computing the phase average of the variables. In summary, for the most general case, the instantaneous velocity $\boldsymbol{v}$ is decomposed as follows:

$$\boldsymbol{v} = \overline{\boldsymbol{v}} + \widetilde{\boldsymbol{v}} + \boldsymbol{v}_w + \boldsymbol{v}', \tag{3}$$

where $\overline{\boldsymbol{v}}$ is the time average velocity, $\widetilde{\boldsymbol{v}}$ is the oscillating phase average velocity (swell), $\boldsymbol{v}_w$ is the wind-waves component (short waves), and $\boldsymbol{v}'$ is the turbulence. See, e.g., Clavero et al. [36] for the definition of the different terms in eq. (3).

In the present scenario, the time average of each of the three last terms in eq. (3) is null. For the swell-only case without wind (exp. 2), the wind-wave contribution is null. For the wind-wave-only case without swell (exp. 1), the phase average term is not defined.

Separation between wind-waves and turbulence is even more tricky.

To address the decomposition in eq. (3), in the present analysis we use "snapshot" proper orthogonal decomposition (POD) (Sirovich [43]) to search for the eigenvalues and eigenvectors that allow us to optimally describe the space of velocities (geometric and in time). The details can be retrieved in Clavero et al. [36], where it was applied for three-dimensional particle tracking velocimetry in a volume of measurement in a pre-breaking wave, and in the Appendix B.

Figure 6 is a snapshot of exp. 3, representing the instantaneous vector velocity field in the $x - y$ plane (red vectors), the oscillating phase average vector velocity field (dark grey vectors), and the instantaneous transverse velocity (coloured shaded areas).

In the data presentation and analysis, we also refer to the correlations between the variables to define a Reynolds oscillating component tensor as follows:

$$\widetilde{\mathbf{A}} = - \begin{bmatrix} \overline{\widetilde{u}\widetilde{u}} & \overline{\widetilde{u}\widetilde{v}} & \overline{\widetilde{u}\widetilde{w}} \\ \overline{\widetilde{v}\widetilde{u}} & \overline{\widetilde{v}\widetilde{v}} & \overline{\widetilde{v}\widetilde{w}} \\ \overline{\widetilde{w}\widetilde{u}} & \overline{\widetilde{w}\widetilde{v}} & \overline{\widetilde{w}\widetilde{w}} \end{bmatrix}. \tag{4}$$

The Reynolds wind-wave tensor is expressed as follows:

$$\mathbf{A}_w = - \begin{bmatrix} \overline{u_w u_w} & \overline{u_w v_w} & \overline{u_w w_w} \\ \overline{v_w u_w} & \overline{v_w v_w} & \overline{v_w w_w} \\ \overline{w_w u_w} & \overline{w_w v_w} & \overline{w_w w_w} \end{bmatrix}, \tag{5}$$

while the Reynolds turbulence tensor results :

$$\mathbf{A}' = - \begin{bmatrix} \overline{u'u'} & \overline{u'v'} & \overline{u'w'} \\ \overline{v'u'} & \overline{v'v'} & \overline{v'w'} \\ \overline{w'u'} & \overline{w'v'} & \overline{w'w'} \end{bmatrix}. \tag{6}$$

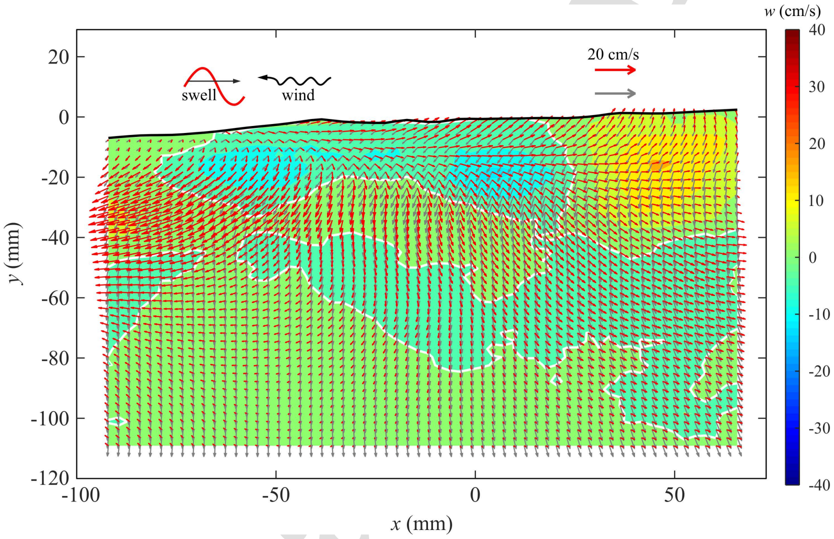

Figure 6: Snapshot of the flow field in exp. 3. The red vectors are the instantaneous velocity, the dark grey vectors are the phase-averaged velocity, the shaded area refers to the transverse velocity w, and the white contour line represents $w = 0$.

The overline indicates a time average, and for some analyses, it should be replaced by the symbol indicating the phase average operator. For simplicity, we will not use any symbol, and variables such as $u'v'$ are intended to be $\overline{u'v'}$ and $\widetilde{u'v'}$ depending on the context.

4. The structure of the oscillating flow field

The general behaviour of the experimental setup was checked by comparing the theoretical distribution of the velocity and the experimental results of the phase average velocity for exp. 2, swell-only, see the details in Appendix C.

An initial assessment of the impact of wind is made by analysing the shape of the wave profile. Figure 7 shows the phase-average profiles for the three experiments in the presence of swell, shifted with the zero value of the phase corresponding to the wave crest. The profile of exp. 2, swell-only, is characterized by high symmetry, with a deviation between the crest and trough amplitude equal to 1% of the wave height. In the case of a wind opposing the swell, as shown in exp. 3, the crest-trough asymmetry is still small, equal to 2% of the wave height, but the difference between the steeper downwind profile and the milder upwind profile is evident. For exp. 4, with the wind following the swell, the crest amplitude is greater than the trough amplitude, with a difference of 4% in the wave height and a modest difference between the two upwind and downwind profiles. In both cases, in the presence of wind the trough is delayed, with a phase $\phi_t > \pi$.

The origin of the asymmetries lies in the dynamics of the short wind-waves and their breaking, which preferentially occurs at the crest of the swell due to the reduction in gravity in the non-inertial system integral to the swell. It is also plausible that breaking is more intense in the case of opposing wind than in the case of following wind. This is one of the numerous implications of breaking, which modifies the momentum flux distribution and generates surface turbulence.

Figure 8 shows a synoptic view of the experimental profiles of the oscillating velocities, $\widetilde{u}, \widetilde{v}$ and $\widetilde{w}$ normalized with respect to the velocity scale $u_{scale} = H_{rms}/T_m$, for three of the four tests (excluding exp. 1, in which only wind-waves are present). The results show a clear effect of the presence of wind for all velocity components, with particular evidence for the transverse component, which is close to zero in exp. 2 (swell-only) and rather high in exp. 3 (wind opposing the swell) and exp. 4 (wind following the swell). The

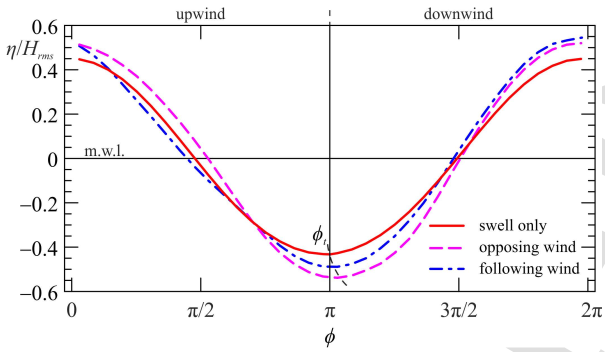

Figure 7: Phase average wave profiles for swell-only (exp. 2), wind opposing swell (exp. 3), and wind following swell (exp. 4). For these two last cases the trough phase is $\phi_t > \pi$.

presence of wind reduces the amplitude of the oscillations near the free surface for both velocity components along the x-axis and along the y-axis. Additionally, there is a shift of the maxima below the free surface, with a modest phase shift and asymmetry which are already visible in the phase-average wave profiles in figure 7.

An important comparison relates to the time average velocity profiles, calculated in the fixed reference system to capture the Stokes drift for consistency of comparison with literature data. Figure 9 shows the results for the four experiments. A mean nonzero horizontal velocity current $\overline{u}$ is evident in exp. 1 (wind-waves-only), as shown in figure 9a, with modest contributions from the other two velocity components. The maximum is below the minimum level of the interface, followed by a change in sign at $y \approx -4$. In the swell-only case, as shown in figure 9b, the theoretical Stokes drift (pink dashed area) is $\approx 25\%$ greater than the measured drift. The return current, for $y < -0.4$, appears to be slightly less than what would be required to balance the Stokes drift (we are neglecting, however, the structure of any recirculation cells). The other two time average velocity components are very small.

Experiment 3, as shown in figure 9c, reveals the joint effect of the wind opposing the swell, with the former significantly reducing the Stokes drift and triggering the other two velocity components. However, these two velocity components are again modest.

Finally, exp. 4, in figure 9d, shows the joint effect of the wind following

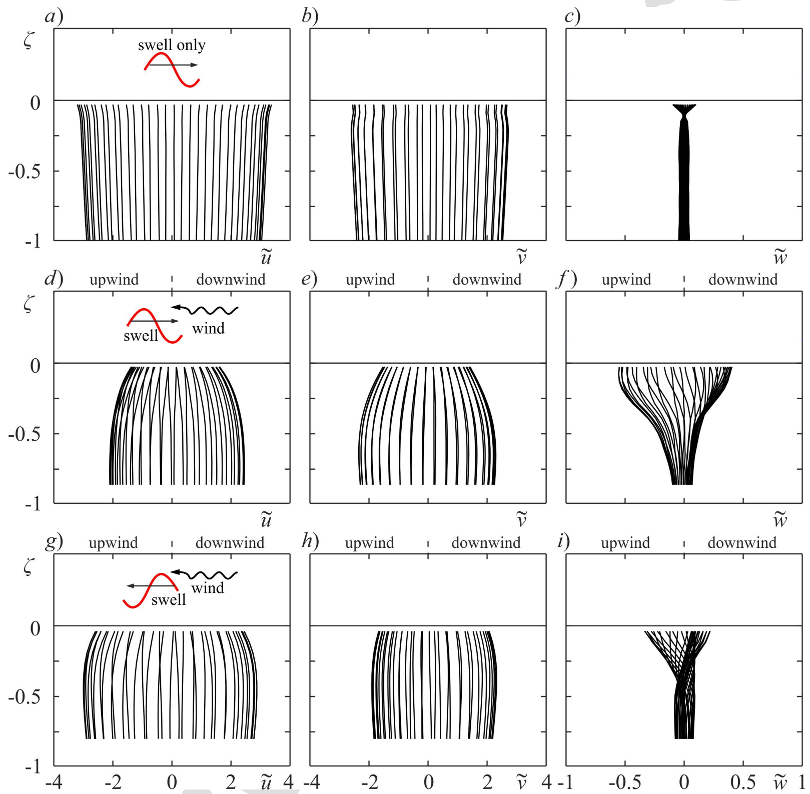

Figure 8: Dimensionless experimental oscillating velocity components. *abc*) Exp. 2, swell-only , *def*) exp. 3, wind opposing a swell, and *ghi*) exp. 4, wind following a swell. The scale of the velocity is $u_{scale} = H_{rms}/T_m$. Velocity profiles are plotted at phase intervals of 10°.

the swell, with a combination of the Stokes drift and wind-generated current leading to a $\approx 50\%$ increase in the maximum horizontal velocity value, with respect to that of exp. 2, just below the mean water level. Again, the two components $\overline{v}$ and $\overline{w}$ take on small but not negligible values, confirming the presence of a three-dimensional structure of the flow field, with currents in all three directions.

Figure 10 shows the vertical profiles of the OKE, $\widetilde{\kappa}$, and the correlations of the oscillating components. In the swell-only case, as shown in figures 10*a*, the contribution of the transverse component to the OKE appears to be modest and $\widetilde{\kappa}_x > \widetilde{\kappa}_y$. In the case of the wind opposing a swell, figure 10*b* shows that the two components of horizontal and vertical OKE are almost equal, with the transverse component almost negligible and with a tiny contribution only near the interface. The value of $\widetilde{\kappa}$ near the free surface is $\approx 25\%$ of the value measured in exp. 2 (swell-only), although the difference decreases for increasing depth. In the case of the wind following a swell, as shown in figure 10*c*, the vertical component of the OKE is almost half the horizontal component, increasing the difference with respect to exp. 2, and the contribution of the transverse OKE appears to be modest. The OKE is $\approx 50\%$ of the value measured in exp. 2. These results are consistent with the model proposed by Hasselmann [44], in which swell is globally attenuated by the compresence of short wind-waves, regardless of their relative direction of propagation, in an energy balance in which the radiation stress gradient extracts energy from swell. This mechanism appears more efficient in exp. 3, with the wind opposing the swell, than in exp. 4, with the wind flowing along the swell. There are also two more effects which can be responsible of the attenuation, the straining of turbulence by the Stokes drift (Teixeira and Belcher [45], Ardhuin and Jenkins [46, 47]) and the viscous dissipation at the air-sea interface (Dore [48]).

Figure 10*d* shows that the diagonal terms for exp. 2, theoretically null for progressive waves, are nearly null experimentally except for $-\widetilde{u}\widetilde{v}$, which acts uniformly in the vertical direction and transfers momentum downwards. Similar results were obtained in the PW1-7 experiments in Addona et al. [27] for regular waves in the presence of reflection, indicating that even small reflections (in the present experiment, the absorption system results in a tiny but nonzero coefficient of reflection equal to 0.05) can be effective in modulating the Reynolds wave shear stress. In the other two experiments, as shown in figure 10*ef*, the effect of the wind, combined with a small but

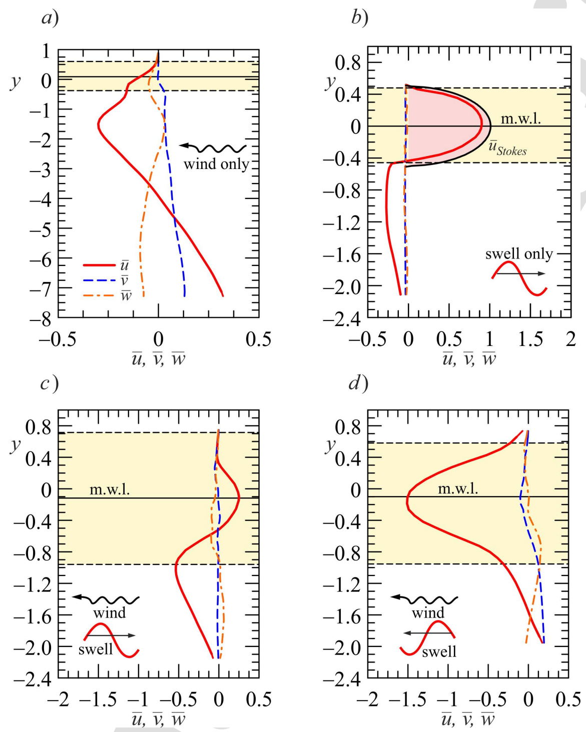

Figure 9: Time average velocities, *a*) for exp. 1 (wind-waves-only), *b*) for exp. 2 (swell-only), *c*) for exp. 3 (wind opposing a swell) and *d*) for exp. 4 (wind following a swell). The yellow dashed areas represent the range of variation of the free surface, with an average maximum and minimum plus two standard deviations; the pink dashed area in *b*) represents the theoretical Stokes drift $\overline{u}_{Stokes}$. These results refer to measured data in the fixed frame, with the vertical coordinate y normalized with respect to H_{rms} with origin at the still water level, and with velocity normalized with respect to $u_{scale} = H_{rms}/T_m$.

nonzero reflection, modulates all three diagonal terms, with the stresses associated with the transverse direction also clearly participating in the balance. A comparison with the WW1-7 experiments in Addona et al. [27] (not shown here), in which wind action was included (although the reflection coefficient was deliberately higher than that in the present experiments), is also helpful. We are not surprised that the variation along the vertical direction appears different between the tests carried out in Addona et al. [27] and the present experiments, considering both the different frames adopted (mobile in the present experiments, fixed in Addona et al. [27]) and the position of the highest measuring volume in Addona et al. [27], which was below the trough.

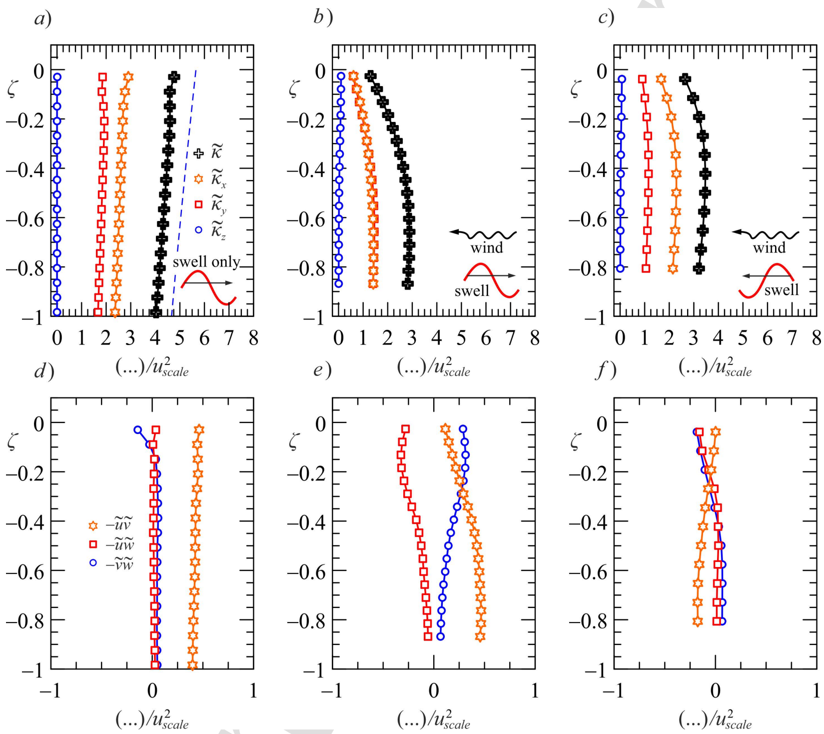

Figure 10: Correlation between the oscillating velocities. *abc*) Oscillating kinetic energy components $\widetilde{\kappa}_x = \widetilde{u}\widetilde{u}/2, \widetilde{\kappa}_y = \widetilde{v}\widetilde{v}/2, \widetilde{\kappa}_z = \widetilde{w}\widetilde{w}/2$ and total kinetic energy $\widetilde{\kappa} = \widetilde{\kappa}_x + \widetilde{\kappa}_y + \widetilde{\kappa}_z$, and *def*) correlations $-\widetilde{u}\widetilde{v}, -\widetilde{u}\widetilde{w}$ and $-\widetilde{v}\widetilde{w}$ for exp. 2 (swell-only), exp. 3 (wind opposing a swell) and exp. 4 (wind following a swell). The dashed line is the theoretical value of $\widetilde{\kappa}$ for exp. 2. The data were normalized with respect to $u_{scale} = H_{rms}/T_m$.

In conclusion, the results seem to be consistent with the theoretical models, with a sufficiently stringent experimental verification for exp. 2 (for which the analytical solution is available, see the Appendix C), both in terms of the phase average periodic oscillating components of the velocity and the time average velocity. The information of greatest interest relates to the wind-induced alteration of the phase between the oscillating components of swell, resulting in momentum fluxes similar to those associated with the presence of reflected components.

5. The structure of the Reynolds wind-waves tensor

A relevant result of the present experiments is the evidence of a dominant role of the spanwise dynamics if wind is present. This aspect was strongly suspected since wind-waves are initially short crested and then evolve, becoming long crested, with a mechanism of coalescence and energy transfer in the spanwise direction to smooth the energy and momentum gradients. However, to the best of our knowledge, the literature lacks a detailed analysis.

Figure 11 shows the time-averaged vertical profiles of the three components of the WKE and their sum. In all three experiments, the κ_{wx} and κ_{wy} components are quite comparable, and κ_{wz} contributes the most to the layer near the free surface and then decays rapidly; the two components κ_{wx} and κ_{wy} increase below the free surface, presumably receiving energy from the transverse component κ_{wz} according to the principle of energy equipartition but also from the vortex stretching exerted by the shear of the swell flow field. The three components of WKE reach an equal value at depths $\zeta \approx -1.5$ for the wind-only case and $\zeta \approx -0.3$ for the wind opposing the swell case, respectively, with further evolution towards a two-component structure of the tensor, with κ_{wz} fast decreasing. The behaviour is also very similar for the case of wind following the swell, as shown in figure 11c, where a smaller contribution of κ_{wz} and a faster exchange between the three components are observed, with the equality of the three components reached at $\zeta \approx -0.15$. The presence of a swell increases the energy of the wind-waves compared to the wind-only case, and also affects the decay rate. The decay of κ_w with depth is $\propto (-\zeta)^{-1.50}$ for the wind-waves-only, is $\propto (-\zeta)^{-0.70}$ for the wind opposing the swell, and is $\propto (-\zeta)^{-0.56}$ for the wind following the swell. Figure 11d shows the comparison of κ_w for the three configurations, with an evident increment of the wind-waves energy if a swell is already present, in

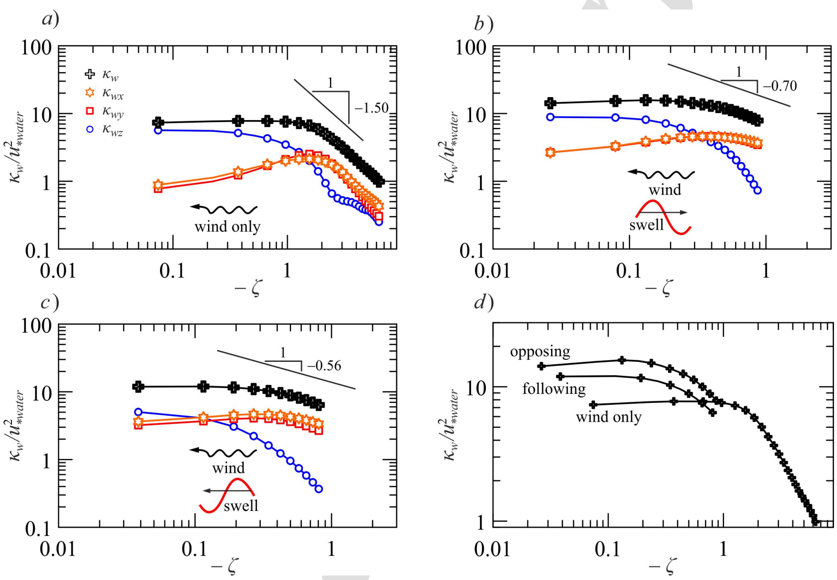

Figure 11: Vertical profiles of the nondimensional WKE components. *a*) Experiment 1 with wind-waves-only, *b*) exp. 3 with wind opposing the swell, *c*) exp. 4 with wind following the swell, *d*) κ_w comparison for the three experiments.

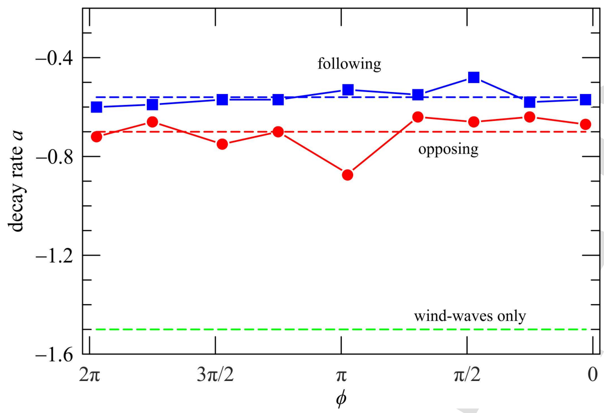

Figure 12: Decay rate a for the WKE at different phases, $\kappa_w \propto (-\zeta)^a$. The dashed lines refer to the decay rate for the average WKE vertical profile.

particular for the opposing wind case. Numerous factors justify the differences between the three configurations: the presence of a swell induces vortex stretching of the eddies associated with the wind-waves, with a consequent energy transfer that partially offsets the non-linear energy transfer from the short wind-waves to the swell.

A further analysis refers to the decay rate of κ_w as a function of the phase, as shown in figure 12 (in the wind-wave-only case, the WKE does not depend on the phase). The two cases of wind opposing/following a swell show very similar decay rates at the crest ($\phi = 0$) and significantly different decay rates at the trough ($\phi = \pi$). We could not find an interpretation. It can be conjectured that the effect of wake separation at the crest is amplified in the case of opposing wind and gives rise to a more pronounced alternation of WKE generation than in the case of following wind, with a sheltering effect and a faster decay at the trough. However, we do not have all the information needed to write the energy balance equation to interpret the overall dynamics of WKE.

As a final step, table 2 lists the distribution of the WKE time averaged in layer $-1 < \zeta < 0$. There is again evidence that the presence of a swell reduces the transverse component κ_{wz}, forcing isotropy in the Reynolds wind-wave tensor for the wind opposing configuration (the three terms are 1/3 of the total) and favouring an almost two-dimensional structure (with minimum energy in the transverse direction) for the wind following configuration. Recall

Flow configuration	$u_w u_w$	$v_w v_w$	$w_w w_w$
exp. 1 wind-waves-only	0.22	0.22	0.56
exp. 3 wind opposing	0.33	0.33	0.34
exp. 4 wind following	0.44	0.38	0.18

Table 2: WKE distribution, time average values in the layer $-1 < \zeta < 0$.

that one of the main contributors to the transfer of energy between larger and smaller scales is the vortex stretching imposed by the swell strain tensor on the small eddies of the wind-waves components. It clearly acts differently depending on the wind direction.

Comparison with other experiments in the literature is somewhat difficult given the mobile frame chosen here, while the available data in the literature are in a fixed frame of reference, with the probes sampling in a fixed position in space. In fact, a fixed probe in space records the effects of level changes over time, with a varying distance of the sampling volume from the interface, and should reduce the values of the estimated variables to some extent compared to those obtained by measuring at constant depths relative to the interface, as we do in the present experiments. In addition, in most experiments in the literature, the first volume of measurements is below the trough of the wave, with some missing fundamental information on the dynamics between the trough and the crest.

In summary, the comparison between the different configurations, which are all comparable with respect to the air friction velocity, shows that (i) the wind-waves force dominant spanwise dynamics, with WKE levels in the z-direction that are two or three times those of the WKE components in the other two directions, at least in the boundary layer beneath the interface; (ii) the opposing wind, in exp. 3, induces slightly higher levels of wind-waves kinetic energy than those in the following wind case in exp. 4; (iii) the wind-waves-swell coupling amplifies the wind-waves energy with respect to the wind-wave-only case.

6. The structure of the Reynolds turbulence stress tensor

An analysis similar to that conducted for the wind-waves components was also carried out for the turbulence. For the swell case only, turbulence (and vorticity) arises from the shear immediately below the air-water interface. In all other cases, the wind action mainly generates it, mostly due to breaking of the wind-waves. As usual, this scenario is the result of the processes of production, diffusion and advection driven by the many forcings, up to and including dissipation.

Figure 13 shows the vertical profiles of the time average TKE, of both the three components and their sum.

A comparison of the results of the wind-only test with those of similar experiments in Magnaudet and Thais [49], with comparable friction velocities, shows that their $\kappa \approx 8.2$ is greater than $\kappa \approx 2$ at $\zeta \to 0$ in the present experiment. ($\kappa \approx 8.2$ is computed by observing that their measurements at the point closest to the interface are $(\overline{u'^2})^{1/2}/u_* \approx 2.5$, $(\overline{w'^2})^{1/2}/u_* \approx 2$, and $(\overline{v'^2})^{1/2}/u_* \approx 2.5$ for the horizontal, vertical, and transverse root mean square components, respectively, with $u_* \equiv u_{*water}$; see figure 7abc in Magnaudet and Thais [49], where they adopted w and v for the vertical and transverse velocity component, respectively.) The ratio between the three components is also different since, in Thais and Magnaudet [41] experiments, $\kappa_x \approx \kappa_z$ and κ_y is 35% smaller than the other two, while in the present experiment, κ_z is much larger than the other two components. A comparison with the results of Experiment E1 (only wind) in Thais and Magnaudet [33] shows that for the wind-only experiment, in the absence of the swell, the level of turbulence in the present experiment is lower, $\kappa \approx 2$, than their value $\kappa \approx 20$ (see their figure 3). Cheung and Street [24] for the horizontal and vertical components alone, found $k_x \approx 5.1$ ($(\overline{u'^2})^{1/2}/u_* \approx 3.2$ in their figure 2) and $k_y \approx 1.3$ ($(\overline{v'^2})^{1/2}/u_* \approx 1.6$ in their figure 3). These two TKE components sum to 6.4, which is much larger than the $\kappa_x + \kappa_y \approx 0.6$ found in the present experiment. Longo et al. [50] found $\kappa_x \approx 4.2$ and $\kappa_y \approx 3$ at $\zeta \approx -0.15$ (see their figure 10), again a value larger than the value found in the present experiments.

The decay of κ with depth is $\propto (-\zeta)^{-0.80}$, similar to the decay $\propto (-\zeta)^{-0.9}$ found for E1 in Thais and Magnaudet [33] and much less rapid than the decay $\propto (-\zeta)^{-1.3}$ in Thais and Magnaudet [41].

This behaviour is most evident for exp. 2 in figure 13b (swell-only), with a fast decrease in all three components in the $-0.1 < \zeta < 0$ boundary layer. The TKE is mainly along $z-$axis direction, and then it is shared among the three components at $\mathcal{O}(0.1)$. The decay of κ (mainly the decay of κ_z) with depth is $\propto (-\zeta)^{-1.22}$, which is the fastest among the four experimental

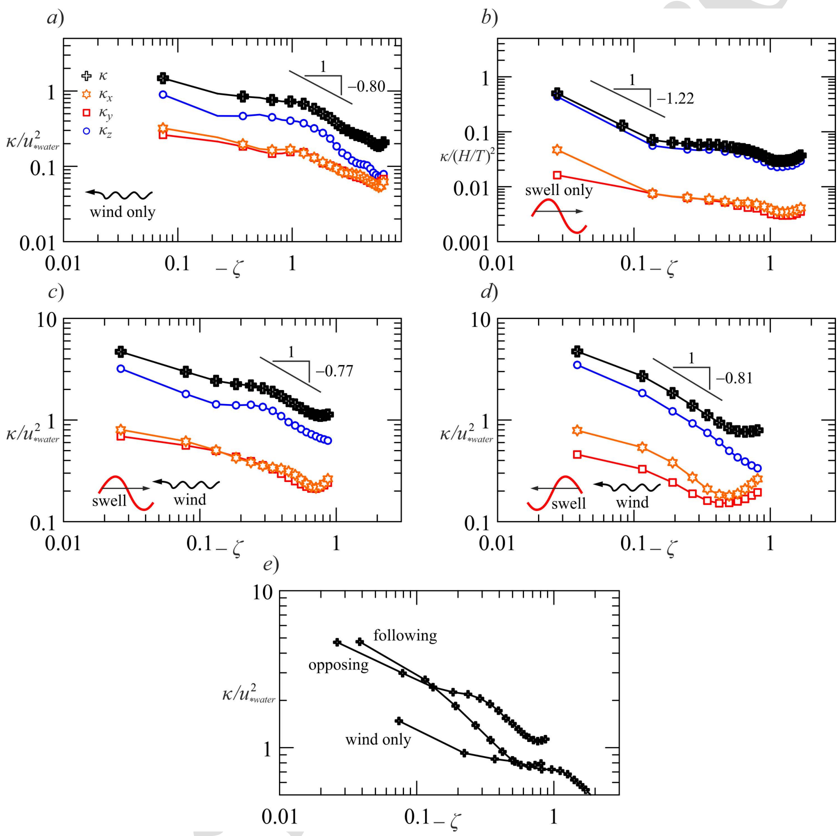

Figure 13: Vertical profiles of the nondimensional TKE components. *a*) Experiment 1 with wind-waves-only, *b*) exp. 2 with the swell-only, *c*) exp. 3 with wind opposing the swell, *d*) exp. 4 with wind following the swell, *e*) comparison of $\kappa = \kappa_x + \kappa_y + \kappa_z$ for the three experiments where wind is blowing (expts 1, 3, 4).

conditions.

Various interpretations are possible: one notable aspect is the different widths of the channels, given that the evolution of wind waves is never purely two-dimensional. Additionally, the presence of active absorption, as opposed to the passive absorption of the experiments in the referenced papers, inevitably modifies the flow field. Furthermore, the different wave age affects the number of breaking waves and, consequently, the turbulent energy.

Figure 13c refers to wind opposing a swell. There are few data in the literature reporting measurements similar to the present one for swell with opposing wind. As an approximate guideline, we can consider Experiment 4 in Addona and Chiapponi [29], for which a reflection of approximately 13% is documented and for which the turbulence also includes fluctuations induced by wind-waves. The first useful measurement point, after scaling the variables as in the present tests, is at $\zeta \approx -0.82$, where their value of $\kappa_x + \kappa_y \approx 1.3$ compares to the value of the present experiment of approximately 1.7 (but the wind fluctuation contribution equals ≈ 5.5; see figure 11b). The decay of κ with depth is $\propto (-\zeta)^{-0.77}$, with faster decay for the κ_z component and slower decay for the other two components κ_x and κ_y.

The decay rate for exp. 4 in figure 13d (wind following the swell) is $\propto (-\zeta)^{-0.81}$, which is slightly faster than that for the swell and opposing wind and quite similar to that of the wind-wave-only experiment.

Figure 13e compares the profiles of κ for the three experiments where wind is present. As already observed for the WKE, the TKE is enhanced by the presence of the swell with respect to the wind only case. The values of TKE for the wind following/opposing cases are almost equal near the free surface, but the decay coefficient with depth is quite different.

Figure 14 shows the decay coefficient of κ at different phases for the four experiments (in the wind-wave-only case, the TKE and its decay do not depend on the phase). The swell-only case shows great variability. The wind opposing the swell case shows a minimum (absolute) decay rate on the upwind side ($3\pi/2 < \phi < \pi$) and a maximum decay near the downwind side, while the wind following the swell case shows a maximum decay rate on the downwind side.

The decay along the vertical of turbulence is the result of momentum and TKE fluxes, as well as the generation and dissipation of TKE. A slower decay indicates more uniform generation or less effective dissipation and transfer.

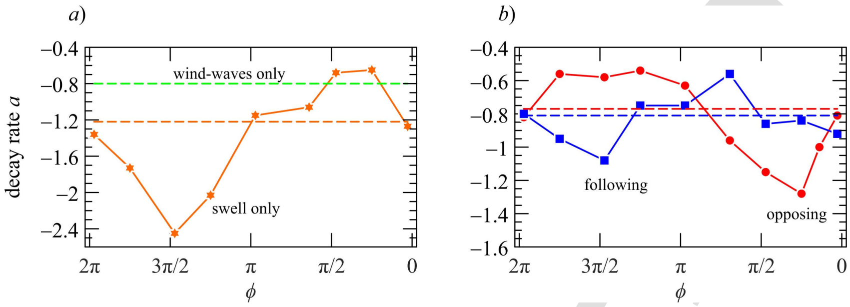

Figure 14: Decay rate a with depth for TKE at different phases, $\kappa \propto (-\zeta)^a$. a) Experiments 1–2 with wind-wave-only and swell-only, b) expts 3–4 with wind opposing/following the swell. The dashed lines refer to the average decay rate for the TKE vertical profiles.

Flow configuration	$u'u'$	$v'v'$	$w'w'$
plane wakes (Townsend [51])	0.43	0.32	0.25
open channel (Nezu and Nakagawa [52])	0.54	0.28	0.17
open channel with a weir (Longo [53])	0.54	0.43	0.03
pre-breaking wave (Clavero et al. [36])	0.55	0.31	0.14
exp. 1 wind-waves-only	0.22	0.20	0.58
exp. 3 wind opposing	0.19	0.17	0.64
exp. 4 wind following	0.20	0.13	0.67

Table 3: TKE distribution in different flow configurations. The values by Townsend [51] refer to plane wakes; the values by Nezu and Nakagawa [52] refer to the intermediate region of an open channel; the values by Longo [53] are beneath a fluctuating free surface; and the values by Clavero et al. [36] are beneath a wave in pre-breaking condition on a berm. Data for the present experiments are averaged in the layer $-1 < \zeta < 0$.

The available data allow us to conclude that the average decay coefficient is little different for the three experiments in which the wind is present, with values between -0.75 and -0.8, which are lower for the two cases in which the wind follows/opposes the swell. The variability during the phase, on the other hand, appears to be quite different in the two cases where swell and wind are present. No simple interpretation was found on the basis of our measurements.

To get an idea of the variability of the distribution of TKE components along the three directions, table 3 reports the values of the TKE distribution documented in literature for different flow fields and for the present experiments. Obviously, different flow configurations result in very different turbulence structures.

In summary, the comparison between the different configurations indicates that the spanwise component is dominant. The two cases of wind opposing/following the swell (expts 3–4) show similar turbulence levels, with turbulence more persistent with depth for exp. 3. The coupling between wind-waves and swell amplifies the turbulence with respect to the wind-waves-only case.

7. Kinetic energy distribution

To conclude the analysis of kinetic energy budget, we report in figure 15 a comparison of the OKE, the WKE and the TKE. The important role of short wind-waves, which dominate all other components in the analysed layer, is quite evident. In the case of the wind-waves-only in figure 15a (with a scaled velocity equal to the ratio H_{w-rms}/T_{w-rms}), it is possible to estimate the depth of diffusion of wind-waves fluctuations, with the WKE always at least one order of magnitude larger than the TKE almost constant in $-1 < \zeta < 0$. As expected, for the swell-only case, in figure 15b energy is almost entirely OKE with small TKE contribution immediately beneath the air-water interface. The wind-waves generated by a wind opposing/following the swell, as shown in 15cd, contain more than 50% of the total kinetic energy, with the TKE equal to the OKE only near the interface, and then rapidly decreasing with depth.

Figure 16 shows the same data as a function of the phase, with the values averaged over a layer of thickness ≈ 0.2 beneath the free surface. Only expts 3 and 4 are shown since they are the most relevant.

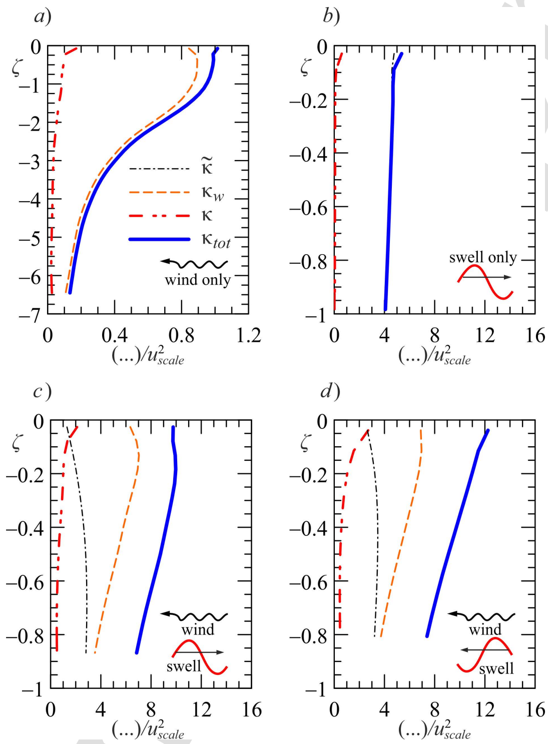

Figure 15: Kinetic energy content for the four different experiments. *a*) Experiment 1 with only wind-waves, *b*) exp. 2 with swell-only , *c*) exp. 3 with swell and opposing wind, *d*) exp. 4 with swell and following wind. Values are dimensionless with $u_{scale} = H_{rms}/T_m$ except for only wind case, where $u_{scale} = H_{w-rms}/T_{w-rms}$. The blue curve refers to $\kappa_{tot} = \widetilde{\kappa} + \kappa_w + \kappa$.

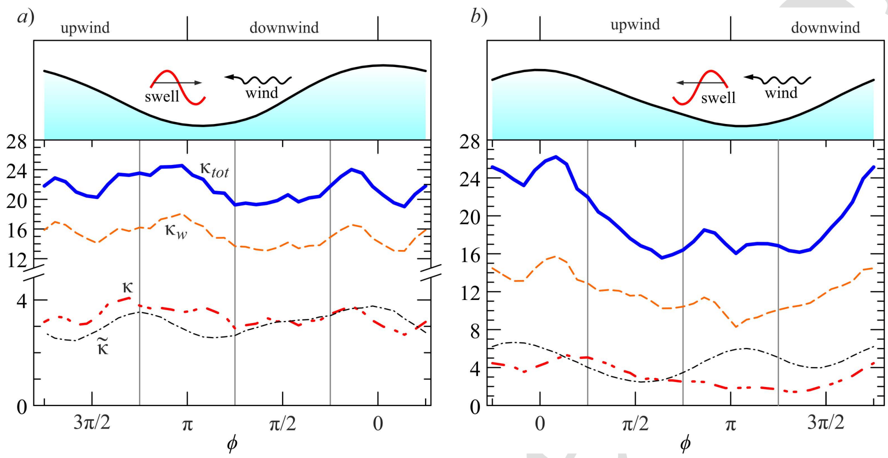

Figure 16: Energy content in the layer of thickness ≈ 0.2 beneath the free surface for *a*) exp. 3, and *b*) exp. 4.

For the wind opposing the swell (exp. 3), as shown in figure 16*a*, the OKE has a maximum at the crest and a second maximum that is shifted towards the node on the upwind side, while the WKE increases at the crest and decreases on the downwind side, presumably due to breaking. It then increases again in the trough, where it reaches its maximum value. The TKE is in phase with the WKE, and the total kinetic energy has maxima in the trough and in the crest.

For the wind following the swell (exp. 4,), as depicted in figure 16*b* the OKE has a maximum in the trough and crest, while the WKE has a maximum in the crest and a minimum in the trough. The TKE appears to lag behind the WKE. The total kinetic energy has a maximum in the crest and a minimum in the trough.

In both experiments, there is evidence of the modulation of the wind-waves with the phase (Phillips [54], Longuet-Higgins [55]), which is significantly different for opposing/following wind.

8. Conclusions

The measurements of the water velocity with a stereo PIV made it possible to analyse precisely, without any assumptions, the complex flow field that dominates the vast majority of wave regimes in the real sea, i.e., swell resulting from the evolution and reorganization of short wind-waves and, in addition, short wind-waves locally generated. The experiments refer to regular waves generated by a paddle in a flume, colinear to waves generated directly by the wind in the overlying wind tunnel, the former reproducing a swell and the latter reproducing short wind-waves. The present data analysis is based on a wave-following moving frame. This frame was selected to observe in detail the physical processes and to compute the values of the variables without the expected distortions induced by the presence/absence of water. We suggest the adoption of this moving frame whenever possible, to favour comparison between different experiments.

The experimental oscillating velocity profiles of the periodic component in the presence of wind and swell (expts 3–4) show lower values than those in the swell-only case, as predicted by Hasselmann's model (Hasselmann [44]). The corresponding OKE immediately beneath the free surface is reduced to $\approx 25\%$ and to $\approx 50\%$ the value with swell-only, respectively, for the opposing and following wind cases. There are two mechanisms that, in addition to the process described by Hasselmann, can be responsible of the attenuation, (i) the straining of turbulence by the Stokes drift (Teixeira and Belcher [45], Ardhuin and Jenkins [46, 47]), and (ii) the viscous dissipation at the air-sea interface (Dore [48]).

The WKE has a structure in which the transverse component dominates, in the layer closest to the free surface, over the other two components. On average, WKE accounts for slightly less than 60% and 55% of the total energy (sum of OKE, WKE and TKE) for the two cases of wind opposing and wind following the swell, respectively. The wind action is significantly enhanced by the presence of swell, and the WKE decays with depth according to a power law function faster for wind opposing than for wind following the swell; in both configurations, the WKE decays more slowly than in the wind-wave-only case. The decay rate is only slightly affected by the phase of the swell.

The transverse component of the TKE always appears to be dominant over the other two components. The comparison of the TKE components with some classical flow fields shows a unique behaviour of the boundary layer below the free surface of the swell, as measured in the present experiments.

The comparison of the contributions to total kinetic energy for expts 3–4 in layer $-1 < \zeta < 0$ indicates that WKE is almost twice the OKE, although the WKE in exp. 1 (wind-waves-only) is only 20% of the OKE in exp. 2

(swell-only). This is a key element of the wave growth process due to energy transfer from wind to water. In essence, the fluctuations due to short wind-waves, which are much more energetic than TKE and OKE, drain part of the OKE; they accumulate energy, which subsequently returns to swell via nonlinear interactions, increasing the height and length and the period of the swell. In this process, wind-waves breaking increases TKE with subsequent energy dissipation and WKE reduction, but the balance is still positive and results in a transfer from WKE to OKE. The oscillatory components of the flow field accounting for OKE are notoriously low-dissipative and therefore increase progressively their energy.

The present study helps clarify and quantify these energy exchanges and sheds light on the mechanisms of interaction between short wind-waves and swell.

Acknowledgements

Funded under the National Recovery and Resilience Plan (NRRP), Mission 4 Component 2 Investment 1.3 - Call for tender No. 341 of 15/03/2022 of the Italian Ministry of University and Research funded by the European Union- NextGenerationEU. Award number: PE00000005, Concession Decree No. 1522 of 11/10/2022 adopted by the Italian Ministry of University and Research, D43C22003030002, "Multi-Risk sciEnce for resilienT commUnities undeR a changiNg climate" (RETURN) - Cascade funding - Spoke VS1 "Acqua", Concession Decree No. 2812 of 09/01/2024 adopted by the General Director of Politecnico di Milano, "Mitigation and Adaptation in Resilient Coastal and estUarine integrated unitS" (MARCUS).

Declaration of Interests

The authors report no conflicts of interest.

f	frequency
h	still water depth
H_{rms}	root-mean-square height of the wave
H_m	nominal wave height
H_{w-rms}	root-mean-square wind-waves height
k	von Kármán constant
K_r	reflection coefficient
L_{exp}	experimental wave length
n	wavenumber
T_m	nominal wave period
T_{w-rms}	root-mean-square period of the wind-waves
T	period
t	time
U_w	wind speed
$U_{w\infty}$	asymptotic wind speed
u_{*air}	friction velocity in the air side
u_{*water}	friction velocity in the water side
u_{scale}	scale of velocity
u_{Stokes}	Stokes velocity
$x-y-z$	space coordinates
$u-v-w$	velocity components
y_0	geometric roughness
ζ	dimensionless vertical coordinates (movable wave following frame)
η	free surface elevation
κ	turbulent kinetic energy (TKE)
$\widetilde{\kappa}$	kinetic energy of the oscillating component (OKE)
κ_w	kinetic energy of the wind-waves (WKE)
κ_{tot}	total kinetic energy (OKE+WKE+TKE)
ρ_{air}	air density
ρ_{water}	water density
ϕ	phase

Table .4: List of symbols.

CIAO	Ocean-Atmosphere Interaction flume (Canal de interacción atmósfera-océano)
FOV	field of view
OKE	oscillating kinetic energy (kinetic energy of the periodic wave)
POD	principal orthogonal decomposition
S-PIV	stereo particle image velocimetry
TKE	turbulent kinetic energy
WKE	wind-waves kinetic energy

Table .5: List of acronyms.

Appendix A. Uncertainty analysis

The Ultrasonic water level sensors are based on the time of flight of packets of Ultrasounds. They are corrected for temperature shift and are characterised by an overall accuracy of 0.7 mm in the vertical. The footprint of the Ultrasound cone on the water surface has an average diameter of 10 mm, hence the minimum wavenumber equals $\approx 300\,\mathrm{m}^{-1}$ corresponding to a deepwater waves frequency of $\approx 10\,\mathrm{Hz}$. The Pitot tube has a nominal accuracy of 1% FS, corresponding to $\pm 40\,\mathrm{cm\,s}^{-1}$ for the adopted instrument, with uncertainty in the vertical position of 0.5 mm and misalignment of less than 5°.

A comprehensive analysis of uncertainties in the S-PIV can be found Bhattacharya et al. [56]. According to Bhattacharya et al. [56] the uncertainties originate from a number of factors, beginning with the dewarping of the two cameras, which results in a disparity map and the definition of the uncertainty associated with each disparity vector. Subsequently, the uncertainty in the position of the transverse coordinate, z, must be added, as well as the uncertainty due to the mapping coefficients. Ultimately, the planar uncertainties and the uncertainties in the angles between the axes of the cameras and the plane of measurement are derived, which, when combined, result in the uncertainties for the three velocity components. The results indicate that if a self-calibration procedure is adopted (the procedure adopted in the present experiments) (see Wieneke [57]), the largest uncertainty is the planar uncertainty.

Appendix B. The POD method

The three components of velocity for each snapshot are combined with the velocity of all the other snapshots to create a matrix with a number of elements equal to three times the number of measurement points by the number of snapshots. The eigenvalues and the eigenvectors of this matrix are then computed, in number equal to the number of snapshots, representing the different modes and the corresponding optimal basis. Finally, the coefficients for each set of velocity in a snapshot are estimated, in number equal to the number of modes. The signal can be reconstructed as a linear combination of the elements of the computed modes. The modes, equal to the number of snapshots, are ranked according to their energy contribution, with the most energetic modes carrying the most relevant information on the flow field. Hence, we can separate the flow field by assuming a threshold of energy above which we allocate the turbulence. For the present analysis, we have assumed that turbulence is described by the less energetic modes containing a total of 10% of energy.

Figure Appendix B.1*a*) shows the energy content of the modes for the four tests, with a variegate energy content for the first modes, and figure Appendix B.1*b*) shows the spectrum of the coefficients of the first six modes in exp. 3, with a spike corresponding to the swell, other superharmonics accounting for the non-linearity of the swell, and a bump in the range of the wind-waves.

Appendix C. Comparison between experiments and theory for swell-only

The theoretical profiles were calculated based on linear wave theory, with the experimental values H_{rms} and L_{exp} estimated from the measured water level in sections US4-US5 (cross-correlation of the two signals was adopted for estimating the phase celerity) and the mean water depth during the test. Figure Appendix C.1 shows the comparison, with fairly good agreement for the (dimensionless) horizontal component $\widetilde{u}$ (figure Appendix C.1*a*), with a slight underestimation of the theory compared to the experimental results in the crest and the trough (the scales of the figure axes and colour bars were selected to be as uniform as possible for the variables being compared in the same figure; in some cases, due to the wide range of values represented, it was necessary to modify the scales within the same figure to highlight the

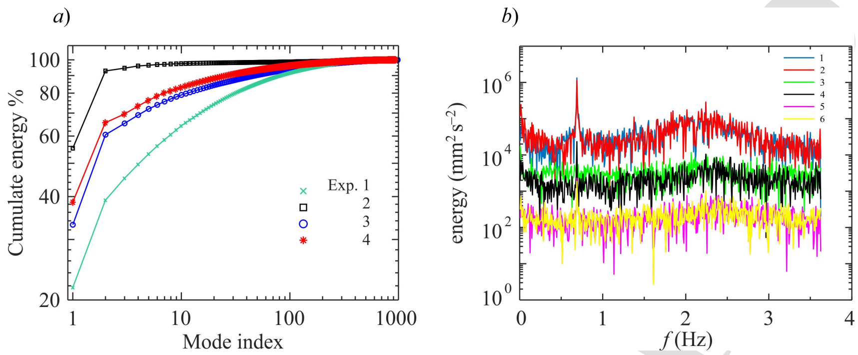

Figure Appendix B.1: Results of the POD. *a*) The cumulative energy of the POD modes for the four experiments, and *b*) the spectral content of the first 6 modes in exp. 3, accounting for more than 70% of the total energy. For ease of viewing, the mode curves, which are shown in pairs, are shifted vertically with a downshift of 10 and 100 mm^2 s^{-2} for modes 3–4 and 5–6, respectively.

differences). For the vertical velocity component $\widetilde{v}$, as shown in figure Appendix C.1*b*, the theory systematically overestimates the maximum values (at the nodes). The transverse velocity component $\widetilde{w}$, shown in figure Appendix C.1*c*, is null in theory (the waves are cylindrical), but experimentally, it is not zero. However, it is almost two orders of magnitude smaller than the other two velocity components and is highly symmetric, which indicates that it is not noise but rather a physical process.

Notably, more pronounced deviations can be obtained immediately beneath the free surface, which can be attributed to several effects: (i) the higher uncertainty of the experimental results near the interface, both for the S-PIV measurements and for the interface identification, and (ii) the presence of vorticity and turbulent components in the surface boundary layer. Other factors that cause discrepancies are the presence of currents and seiches within the channel and the presence of reflected components, albeit modest, in addition to nonlinear effects.

Figure Appendix C.2 shows the comparison at four different depths of the experimental and theoretical velocities with varying phases. This comparison also shows good agreement, with substantial correctness of the phase and values for the horizontal component and a slight phase shift for the vertical component. The transverse component, which is theoretically zero since the wave is two-dimensional, is experimentally nonzero but has values almost

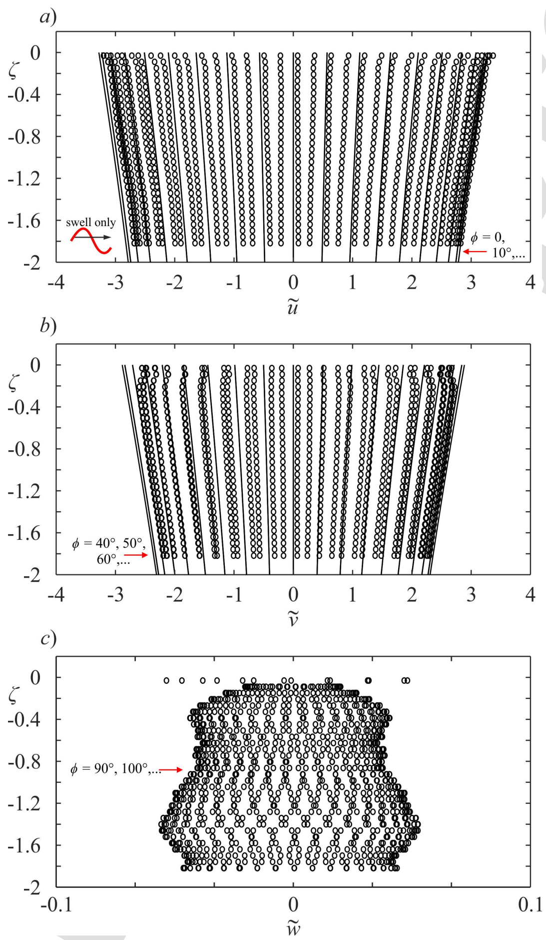

Figure Appendix C.1: Swell-only (exp. 2). Comparison between the experimental results (symbols) and theoretical velocities (curves). *a*) Horizontal velocity, *b*) vertical velocity and, *c*) transverse velocity. Representation for 36 phases, each 10°. Velocities are dimensionless.

two orders of magnitude smaller than those of the other two components and decreases rapidly with depth.

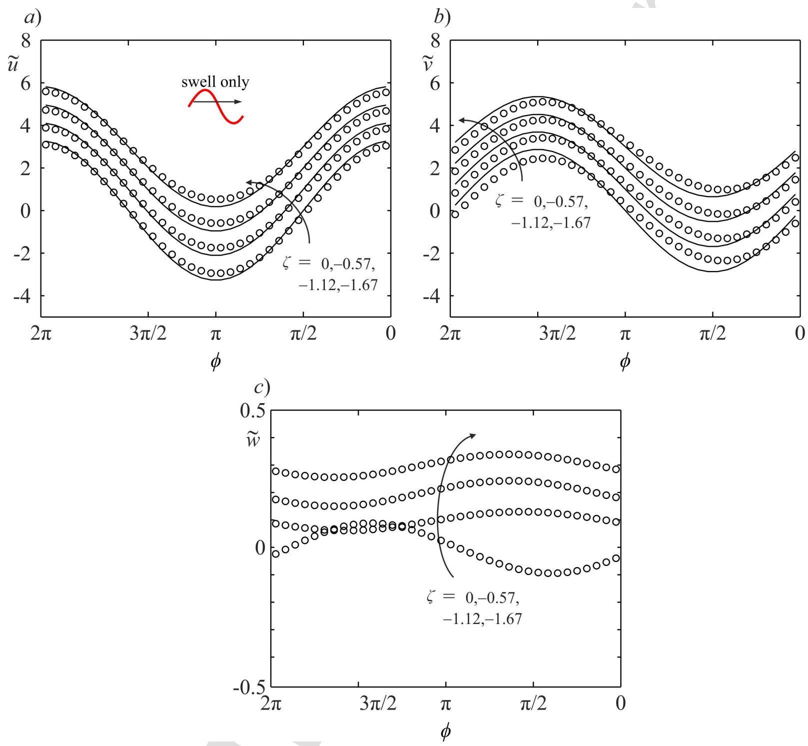

Figure Appendix C.2: swell-only (exp. 2). Comparison of the experimental and theoretical velocities at four depths. *a*) Horizontal velocity, *b*) vertical velocity and *c*) transverse velocity. The symbols are experiments, and the curves are theory. The values are shifted by one unit for $\widetilde{u}$ and $\widetilde{v}$ and by 0.1 for the transverse component for ease of visualization. The theoretical velocities for $\widetilde{w}$ are zero.

References

[1] A. Semedo, Atmosphere-ocean interactions in swell dominated wave fields, Ph.D. thesis, University of Uppsala, 2010.

[2] P. P. Sullivan, J. C. McWilliams, Dynamics of winds and currents coupled to surface waves, Annual Review of Fluid Mechanics 42 (2010).

[3] H. Jeffreys, On the formation of water waves by wind, Proceedings of the Royal Society of London. Series A 107 (1925) 189–206.

[4] J. W. Miles, On the generation of surface waves by shear flows, Journal of Fluid Mechanics 3 (1957) 185–204.

[5] O. M. Phillips, On the generation of waves by turbulent wind, Journal of Fluid Mechanics 2 (1957) 417–445.

[6] S. E. Belcher, J. A. Harris, R. L. Street, Linear dynamics of wind waves in coupled turbulent air—water flow. Part 1. Theory, Journal of Fluid Mechanics 271 (1994) 119–151.

[7] M. P. Buckley, F. Veron, Structure of the airflow above surface waves, Journal of Physical Oceanography 46 (2016) 1377–1397.

[8] M. P. Buckley, F. Veron, The turbulent airflow over wind generated surface waves, European Journal of Mechanics-B/Fluids 73 (2019) 132–143.

[9] M. P. Buckley, F. Veron, K. Yousefi, Surface viscous stress over wind-driven waves with intermittent airflow separation, Journal of Fluid Mechanics 905 (2020) A31.

[10] K. Yousefi, F. Veron, M. P. Buckley, Momentum flux measurements in the airflow over wind-generated surface waves, Journal of Fluid Mechanics 895 (2020) A15.

[11] K. Hasselmann, On the non-linear energy transfer in a gravity-wave spectrum part 1. General theory, Journal of Fluid Mechanics 12 (1962) 481–500.

[12] K. Hasselmann, On the non-linear energy transfer in a gravity wave spectrum part 2. Conservation theorems; wave-particle analogy; irrevesibility, Journal of Fluid Mechanics 15 (1963) 273–281.

[13] K. Hasselmann, On the non-linear energy transfer in a gravity-wave spectrum. part 3. Evaluation of the energy flux and swell-sea interaction for a Neumann spectrum, Journal of Fluid Mechanics 15 (1963) 385–398.

[14] K. Hasselmann, T. P. Barnett, E. Bouws, H. Carlson, D. E. Cartwright, K. Enke, J. A. Ewing, A. Gienapp, D. E. Hasselmann, P. Kruseman, et al., Measurements of wind-wave growth and swell decay during the Joint North Sea Wave Project (JONSWAP), Ergaenzungsheft zur Deutschen Hydrographischen Zeitschrift, Reihe A (1973).

[15] H. Mitsuyasu, Interactions between water waves and winds (I): coexistent system of wind wave and regular oscillatory wave, Technical Report, Research Institute for Applied Mechanics, Kyushu University, 1967.

[16] O. Phillips, M. Banner, Wave breaking in the presence of wind drift and swell, Journal of Fluid Mechanics 66 (1974) 625–640.

[17] J. W. Wright, The wind drift and wave breaking, Journal of Physical Oceanography 6 (1976) 402–405.

[18] D. Masson, On the nonlinear coupling between swell and wind waves, Journal of Physical Oceanography 23 (1993) 1249–1258.

[19] G. Chen, S. E. Belcher, Effects of long waves on wind-generated waves, Journal of Physical Oceanography 30 (2000) 2246–2256.

[20] J. Wu, Laboratory studies of wind–wave interactions, Journal of Fluid Mechanics 34 (1968) 91–111.

[21] O. H. Shemdin, Wind-generated current and phase speed of wind waves, Journal of Physical Oceanography 2 (1972) 411–419.

[22] B. M. Howe, A. J. Chambers, S. P. Klotz, T. K. Cheung, R. L. Street, Comparison of profiles and fluxes of heat and momentum above and below an air-water interface, Journal of Heat Transfer 104 (1982) 35.

[23] L. Bliven, N. Huang, S. Long, A laboratory study of the velocity field below surface gravity waves, Gas Transfer at Water Surfaces (1984) 181–190.

[24] T. K. Cheung, R. L. Street, The turbulent layer in the water at an air—water interface, Journal of Fluid Mechanics 194 (1988) 133–151.

[25] W. L. Peirson, A. W. Garcia, S. E. Pells, Water wave attenuation due to opposing wind, Journal of Fluid Mechanics 487 (2003) 345–365.

[26] H. Mitsuyasu, Y. Yoshida, Air-sea interactions under the existence of opposing swell, Journal of Oceanography 61 (2005) 141–154.

[27] F. Addona, A. Lira Loarca, L. Chiapponi, M. A. Losada, S. Longo, The Reynolds wave shear stress in partially reflected waves, Coastal Engineering 138 (2018) 220–226.

[28] F. Addona, L. Chiapponi, M. Clavero, M. Losada, S. Longo, On the interaction between partially-reflected waves and an opposing wind, Coastal Engineering 162 (2020) 103774.

[29] F. Addona, L. Chiapponi, Velocity and stresses of partially-reflected water waves in the presence of opposing wind, Coastal Engineering 183 (2023) 104310.

[30] F. Addona, Interaction between incident and reflected mechanical waves in the presence of an opposing wind, Coastal Engineering (2024) 104572.

[31] S. Elgar, T. Herbers, R. Guza, Reflection of ocean surface gravity waves from a natural beach, Journal of Physical Oceanography 24 (1994) 1503–1511.

[32] A. Baquerizo, M. A. Losada, J. M. Smith, N. Kobayashi, Cross-shore variation of wave reflection from beaches, Journal of Waterway, Port, Coastal, and Ocean Engineering 123 (1997) 274–279.

[33] L. Thais, J. Magnaudet, Turbulent structure beneath surface gravity waves sheared by the wind, Journal of Fluid Mechanics 328 (1996) 313–344.

[34] D. Dabiri, M. Gharib, Experimental investigation of the vorticity generation within a spilling water wave, Journal of Fluid Mechanics 330 (1997) 113–139.

[35] G. L. Wagner, N. Pizzo, L. Lenain, F. Veron, Transition to turbulence in wind-drift layers, Journal of Fluid Mechanics 976 (2023) A8.

[36] M. Clavero, S. Longo, L. Chiapponi, M. A. Losada, 3D flow measurements in regular breaking waves past a fixed submerged bar on an impermeable plane slope, Journal of Fluid Mechanics 802 (2016) 490–527.

[37] S. Longo, M. Clavero, L. Chiapponi, M. A. Losada, Invariants of Turbulence Reynolds Stress and of Dissipation Tensors in Regular Breaking Waves, Water 9 (2017).

[38] F. Addona, Swell and wind-waves interaction under partial reflection conditions, Ph.D. thesis, Università di Parma - Universidad de Granada, 2019.

[39] L. Grare, W. L. Peirson, H. Branger, J. W. Walker, J. P. Giovanangeli, V. Makin, Growth and dissipation of wind-forced, deep-water waves, Journal of Fluid Mechanics 722 (2013) 5–50.

[40] A. Xuan, L. Shen, Analyses of wave-phase variation of Reynolds shear stress underneath surface wave using streamline coordinates, Journal of Fluid Mechanics 931 (2022) A32.

[41] L. Thais, J. Magnaudet, A triple decomposition of the fluctuating motion below laboratory wind water waves, Journal of Geophysical Research: Oceans 100 (1995) 741–755.

[42] M. A. Donelan, F. Anctil, J. C. Doering, A simple method for calculating the velocity field beneath irregular waves, Coastal Engineering 16 (1992) 399–424.

[43] L. Sirovich, Turbulence and the dynamics of coherent structures. Part I, II and III, Quart. Appl. Math. XLV(3) (1987) 561–590.

[44] K. Hasselmann, On the mass and momentum transfer between short gravity waves and larger-scale motions, Journal of Fluid Mechanics 50 (1971) 189–205.

[45] M. A. C. Teixeira, S. E. Belcher, On the distortion of turbulence by a progressive surface wave, Journal of Fluid Mechanics 458 (2002) 229–267.

[46] F. Ardhuin, A. D. Jenkins, On the effect of wind and turbulence on ocean swell, in: ISOPE International Ocean and Polar Engineering Conference, ISOPE, 2005, pp. ISOPE–I–05–301.

[47] F. Ardhuin, A. D. Jenkins, On the interaction of surface waves and upper ocean turbulence, Journal of Physical Oceanography 36 (2006) 551–557.

[48] B. Dore, Some effects of the air-water interface on gravity waves, Geophysical & Astrophysical Fluid Dynamics 10 (1978) 215–230.

[49] J. Magnaudet, L. Thais, Orbital rotational motion and turbulence below laboratory wind water waves, Journal of Geophysical Research: Oceans 100 (1995) 757–771.

[50] S. Longo, D. Liang, L. Chiapponi, L. Aguilera Jimenez, Turbulent flow structure in experimental laboratory wind-generated gravity waves, Coastal Engineering 64 (2012) 1 – 15.

[51] A. Townsend, The structure of turbulent shear flow, Cambridge University Press, 1976.

[52] I. Nezu, H. I. Nakagawa, Turbulence in open channel flows, IAHR Monograph Series, 1993.

[53] S. Longo, Experiments on turbulence beneath a free surface in a stationary field generated by a Crump weir: turbulence structure and correlation with the free surface, Experiments in Fluids 50 (2011) 201–215.

[54] O. M. Phillips, On the attenuation of long gravity waves by short breaking waves, Journal of Fluid Mechanics 16 (1963) 321–332.

[55] M. Longuet-Higgins, A nonlinear mechanism for the generation of sea waves, Proceedings of the Royal Society A 311 (1969) 371–389.

[56] S. Bhattacharya, J. J. Charonko, P. P. Vlachos, Stereo-particle image velocimetry uncertainty quantification, Measurement Science and Technology 28 (2016) 015301.

[57] B. Wieneke, Stereo-PIV using self-calibration on particle images, Experiments in fluids 39 (2005) 267–280.

Highlights

- Stereo PIV is used to measure velocity beneath regular waves in the presence of wind
- The velocity is split into four components: mean, periodic, wind, and turbulent
- The spanwise component dominates the near-surface dynamics when wind is present
- A strong coupling between long waves, short wind waves and turbulence is observed.

Declaration of interests

☒ The authors declare that they have no known competing financial interests or personal relationships that could have appeared to influence the work reported in this paper.

☐ The authors declare the following financial interests/personal relationships which may be considered as potential competing interests: